Solar Physics
DOI: 10.1007/•••••-•••-•••-••••-•

Time Evolution of Force-free Parameter and Free Magnetic Energy in Active Region NOAA 10365

G. Valori[1,2] · **P. Romano**[3] · **A. Malanushenko**[4] · **I. Ermolli**[1] · **F. Giorgi**[1] · **K. Steed**[5] · **L. van Driel-Gesztelyi**[2,6,7] · **F. Zuccarello**[8] · **J-M. Malherbe**[2]

Abstract We describe the variation of the accumulated coronal helicity derived from the magnetic helicity flux through the photosphere in active region (AR) NOAA 10365, where several large flares and coronal mass ejections (CMEs) occurred. We use SOHO/MDI full-disk line-of-sight magnetograms to measure the helicity flux, and the integral of GOES X-ray flux as a proxy of the coronal energy variations due to flares/CMEs. Using the linear force-free field model, we transform the accumulated helicity flux into a time sequence of the force-free parameter α accounting for flares/CMEs via the proxy derived from GOES observations. This method can be used to derive the value of α at different times during the AR evolution, and is a partial alternative to the usual matching of field lines with EUV loops. Combining the accumulated helicity obtained from the observations with the linear force-free theory, we describe the main phases of the emergence process of the studied AR, and relate them temporally with the occurrence of flares/CMEs. Additionally, a comparison with the loop-matching method of fixing alpha at each time independently shows that the proposed method may be helpful to avoid attribution of unrealistic or undetermined val-

[1] INAF Osservatorio Astronomico di Roma, via Frascati 33, 00040 Monte Porzio Catone, Italy
[2] LESIA-Observatoire de Paris, CNRS, UPMC Univ. Paris 06, Univ. Paris-Diderot, 92195 Meudon Cedex, France email: gherardo.valori@obspm.fr
[3] INAF Osservatorio Astrofisico di Catania, Via S. Sofia 78, 95123, Catania, Italy
[4] Department of Physics, Montana State University, Bozeman, MT 59717, USA
[5] Centre for mathematical Plasma Astrophysics, Department of Mathematics, KU Leuven, Celestijnenlaan 200B, 3001 Leuven, Belgium
[6] Konkoly Observatory of the Hungarian Academy of Sciences, Budapest, Hungary
[7] University College London, Mullard Space Science Laboratory, Holmbury St. Mary, Dorking, Surrey RH5 6NT, UK
[8] Dipartimento di Fisica e Astronomia, Universitá di Catania, Via S. Sofia 78, 95123, Catania, Italy

ues of alpha that may originate from an insufficient quality of the image used to identify coronal loops at a given time. As for the relative intensity of the considered events, the linear force-free field theory implies a direct correlation between the released energy on the one hand, and the product of the coronal helicity with the variation of α due to the event on the other. Therefore, the higher the value of the accumulated coronal helicity, the smaller the force-free parameter variation required to produce the same decrease in the free energy during the CMEs.

Keywords: Magnetic fields, photosphere· Velocity fields, photosphere

1. Introduction

It has been established over the past several decades that flares and coronal mass ejections (CMEs), which can influence the whole heliosphere, originate from reconfiguration of magnetic fields and release of free magnetic energy stored in the solar corona. Non-eruptive events, such as confined flares, are also due to the release of free magnetic energy in regions of magnetic field concentrations, *i.e.* in solar active regions (AR). In both cases, the release of the magnetic energy occurs when the nonpotential pre-event state relaxes into a lower energy, possibly nearly potential, post-event state of the magnetic configuration. However, the relationship between the free magnetic energy and the eruptive or noneruptive character of the event is still unknown.

From a different viewpoint, magnetic helicity has been invoked as a key quantity in explaining eruptive events (Kusano *et al.*, 2002). Magnetic helicity is a physical quantity that measures the complexity of the magnetic field (*i.e.*, twist and writhe) and, therefore, it is related to the electric currents present in the magnetic system. Unlike the magnetic energy, helicity cannot be dissipated, since it is nearly perfectly conserved under solar conditions (Berger, 1984). However, the transition from a current-carrying to a nearly potential configuration cannot occur without helicity annihilation and/or helicity ejection. It is speculated that this may happen during CMEs, when the Sun expels from the low corona part of the helicity accumulated in an AR field.

The computation of magnetic free energy and magnetic helicity requires a model of, or at least some assumptions about, the nature of the coronal magnetic field. The simplest possible model is a force-free field, which is justified essentially on the grounds that the corona is magnetically dominated (Forbes, 2000). Because of its magnetic nature, the time scale of variation of the coronal field is much shorter than that of the photosphere, where the coronal field is rooted. Therefore, the coronal field can be described, excluding times where fast events like CMEs occur, as a quasi-static sequence of force-free equilibria, each governed by the equations:

$$\boldsymbol{J} \times \boldsymbol{B} = 0\,, \qquad \nabla \cdot \boldsymbol{B} = 0\,, \tag{1}$$

and driven by the slowly-varying, photospheric boundary conditions. The vanishing of the Lorentz force implies that $\boldsymbol{J} = \alpha \boldsymbol{B}$, and, due to the solenoidal property

of $\boldsymbol{B}$, that the field-line torsion α is constant along individual field lines, but differs in general from field line to field line. That such coronal equilibria must contain currents (and therefore have a finite magnetic helicity) is supported by many observations of twisted coronal structures involved in CMEs, *e.g.*, coronal sigmoids, helical filamentary structures during eruptions (Aulanier and Schmieder, 2002; Török and Kliem, 2005; Romano, Contarino and Zuccarello, 2003). Since α is position-dependent, Equations (1) are nonlinear, and require a map of the three components of the magnetic field (or quantities derived thereof) at the photosphere to be solved (Wiegelmann, 2008; Wiegelmann and Sakurai, 2012). A general solution as a function of the boundary values is not known, and the nonlinear force-free field (NLFFF) equations must be solved numerically (extrapolation). However, the computation of such NLFFF solutions is still a rather demanding numerical effort, requiring the use of the measured transverse components of the field which are intrinsically more noisy and prone to errors than the line-of-sight (LoS) one. There is still no consensus on which is the best method for solving Equations (1), especially when applied to observed boundary conditions which are, in general, not compatible with the force-free assumption (DeRosa *et al.*, 2009). Moreover, the NLFFF extrapolation is not applicable to decades-long series of measurements of the magnetic field of the Sun, which were restricted to LoS measurements only. Therefore, there is still interest in simplified methods of solution.

A major simplification of Equations (1) is to consider α to be finite but constant across field lines (Nagakawa and Raadu, 1972; Seehafer, 1978; Sakurai, 1989). In this case, Equations (1) become linear, and explicit solutions can be built that require only the vertical magnetic field at the photosphere as a boundary condition. For these reasons, linear force-free field (LFFF) models have been extensively applied to build AR coronal models over more than three decades (Mandrini *et al.*, 1996; Schmieder *et al.*, 1996; Mandrini *et al.*, 1997; Démoulin *et al.*, 2002; Green *et al.*, 2002).

On the other hand, the LFFF approximation has several limitations. First of all, in the LFFF approximation, α is a free parameter proportional to the inverse of the longest wavelength in the system. In practice, its magnitude $|\alpha|$ is limited from above by the size of the observed area, with the unphysical result that the current density in the system is limited by geometrical factors rather than by the magnetic field distribution. Moreover, to assume constant value of α implies that currents are filling the entire extrapolated volume, varying continuously like the magnetic field, rather than being concentrated in relatively small volumes as observations seem to indicate. Finally, being a free parameter, α is not determined by the observed magnetic field, and needs to be constrained by additional observations.

Despite its limitations, the LFFF extrapolation method was found to be very useful to describe, for instance, the global topology of AR magnetic field, including the location of bald patches and quasi-separatrix layers (Pariat *et al.*, 2004). As already mentioned, a critical step in the use of LFFF extrapolations is the choice of the free parameter α. A typical method to constrain α is to compare loops identified in EUV images with the field lines obtained by the extrapolated field and projected on the image plane (Green *et al.*, 2002). Such a

loop-matching method finds the value of α at each instant independently of the evolution of the photospheric flux, it is influenced by the accuracy with which loops can be identified in EUV images, and it is in general limited by projection effects. An alternative method to constrain α, but one that requires knowledge of the transverse component of the field at the photosphere, is the so-called "α-best" method (Petsov, Canfield, and Metcalf, 1995), which consists of finding the value of α that minimises the difference between the correspondent calculated transverse component and the observed one. Rather than using the map of the vector field for an NLFFF extrapolation, the best-matching α is then used to compute the linear one. As the for NLFFF extrapolation, the 'α-best' method requires the knowledge of the three components of the magnetic field, which are not always available.

We propose a third method for the determination of the force-free parameter α that is based on the temporal evolution of the magnetic flux. Georgoulis and LaBonte (2007) generalised previous works (Berger, 1985; Démoulin *et al.*, 2002) aimed at identifying the relations between global quantities, like free energy, helicity, and α, within the frame of LFFF theory. In this article, we combine such general relations with the time-dependent helicity accumulated in the coronal field above an AR, as deduced from the horizontal displacements of the photospheric magnetic structures (Chae *et al.*, 2001). Additionally, we introduce a heuristic proxy of the energy liberated in a CME, which is based on GOES observations, and obtain a temporal evolution of α that accounts for drops in free energy due to eruptive events. The method proposed here can be a partial alternative to constrain α when only LoS magnetic field measurements are available. As an example, we apply the method to the evolution of an AR where several flares/CMEs occurred.

The article is organised as follows: In Section 2 we describe the dataset. In Section 3 the analysis of the magnetic flux evolution is reported. In Section 4 we show the method and the results of the magnetic helicity computation. The LFFF approximation and the assumptions used in our method are described in Section 5. A comparison with the EUV loop-matching method is discussed in Section 6. The conclusions are summarised in Section 7.

2. Data Description

AR NOAA 10365 first appeared at the east limb on 21 May 2003 at S04E54 as a relatively dispersed bipolar region. We focus on the emergence that took place right at the east side of this AR, starting on 24 May around 9:00 UT. We analysed full-disk line-of-sight magnetograms acquired by *Solar and Heliospheric Observatory* (SOHO)/*Michelson-Doppler Imager* (MDI; Scherrer *et al.*, 1995) at 6767.8 Å with a spatial resolution of 3.96 arcsec and a time cadence of 96 min from 24 May 2003, at 00:00 UT to 29 May 2003, at 21:35 UT. We selected this time interval, when the longitude of the active region was within within 35° from the disk centre, in order to avoid projection effects in the analysis of the magnetograms. The resulting time series is composed of 88 observations during the selected time interval. We corrected all magnetograms for the angle between

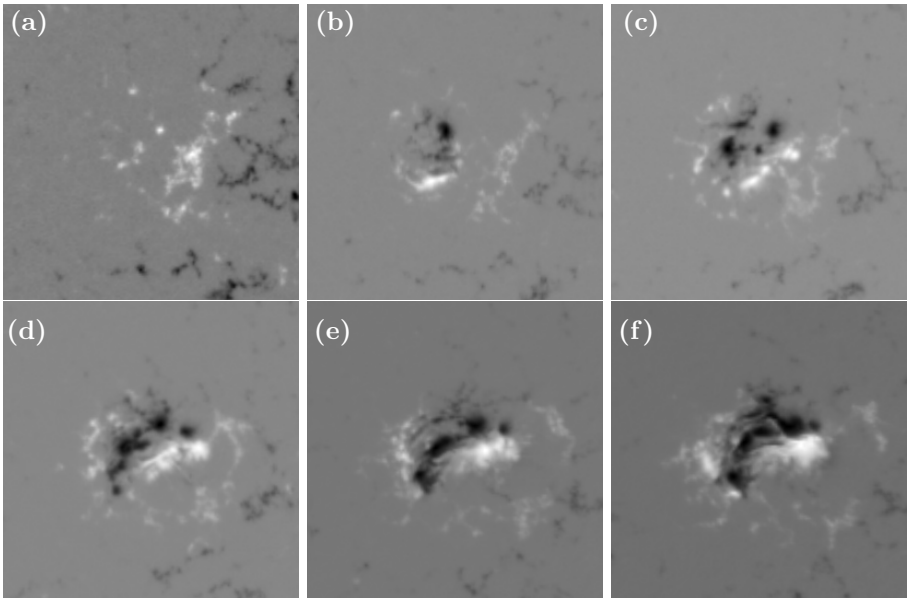

Figure 1. From left to right and from top to bottom, MDI magnetograms showing the magnetic configuration of AR NOAA 10365 at t=5, 25, 50, 75, 100, and 120 h counted from 24 May 2003, 00:00 UT. North is at the top, west is on the right.

Table 1. M and X-class flares occurred in AR NOAA 10365 during its passage over the solar disk. Only the top six events are included in the analysis, as the latter events occurred too close to the limb to be suitable for our analysis. $\Delta\mathcal{E}_c$ is the proxy of the liberated energy as defined in Equation (5).

Number	Day	Start (UT)	Peak (UT)	End (UT)	Φ^{peak}_{GOES} (class)	$\Delta\mathcal{E}_c$ (10^{-2} erg cm^{-2})
1	26 May 2003	05:34	05:50	06:02	M1.9	16
2	26 May 2003	16:22	16:37	16:51	M1.0	9
3	27 May 2003	02:40	03:06	03:21	M1.4	17
4	27 May 2003	05:06	06:26	07:16	M1.6	62
5	27 May 2003	22:56	23:07	23:13	X1.3	66
6	29 May 2003	00:51	01:05	01:12	X1.2	76
7	31 May 2003	02:13	02:24	02:40	M9.3	-
8	1 June 2003	16:43	16:52	06:59	M1.4	-
9	2 June 2003	00:07	00:22	00:43	M6.5	-
10	2 June 2003	08:12	08:37	08:52	M3.9	-
11	2 June 2003	13:13	13:17	13:22	M1.0	-

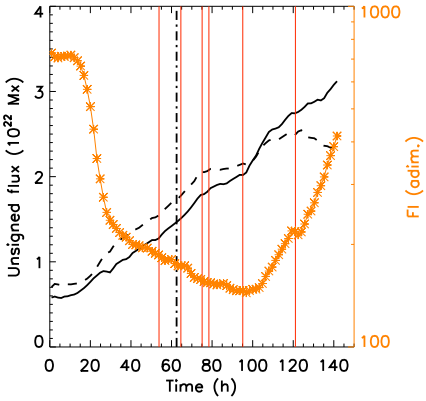

Figure 2. Time evolution of the positive (solid line) and negative (dashed line) magnetic fluxes, and of the function $\mathcal{F}_l$ (connected asterisks) in Equations (2) and (3). The red vertical lines indicate the peak times of the flares in our time series (see Table 1), while the vertical dot-dashed line indicates the time of the central meridian passage of the AR. Time starts at 00:00 UT on 24 May 2003.

the magnetic field direction and the observer's line-of-sight, by supposing that the magnetic field is radial.

We considered subfields of 171 × 171 arcsec centered on the AR and we aligned all subfields by applying a standard differential rotation rate (Howard *et al.* 1990) with a sampling of 1 arcsec (see Romano *et al.* 2011 for more details). We determined the subfield sizes in order to reduce to less than 15% the magnetic flux imbalance between the two polarities. In Figure 1 MDI-snapshots of the evolution of the vertical magnetic field of the AR at different times are shown. Several C, M, and X-class flares occurred in the AR during its passage over the solar disk (see Table 1). All of these flares are temporally correlated with CMEs observed by the *Large Angle Spectroscopic Coronagraph* (LASCO; Brueckner *et al.*, 1995) C2 coronagraph and reported by the SOHO/LASCO CME catalog ($http://cdaw.gsfc.nasa.gov/CME\_list/$). Only the first six events reported in Table 1 occurred during the selected observation interval.

3. Magnetic Flux Evolution

The temporal evolution of the positive and negative magnetic fluxes in the considered subfields is shown in Figure 2. Before the emergence starts (Figure 1a) the region is occupied by the eroded remnants of AR NOAA 10365, whose dispersed flux is only partially included in the selected field of view (FoV). At this time, the balance in the region is slightly dominated by a negative component, which is never entirely removed from the FoV during the evolution of the AR. The emergence starts as a north-south oriented bipole (Figure 1b) within the easternmost trailing positive polarity of the pre-existing flux, around t=10 h (in all plots, time is given in hours starting from 24 May 2003, at 00:00 UT).

The bipole rapidly evolves into more east-west orientation, with the positive polarity as the leading one (anti-Hale orientation for the south hemisphere in cycle 23), in this way inhibiting cancellation with the following positive polarity of the pre-existing flux. Traces of positive polarity to the east of the negative one are also present, possibly a manifestation of a very deformed and weak tongue (Luoni *et al.*, 2011). The flux imbalance in this initial phase of the emergence is about 20%. After this very initial stage, the AR keeps growing by emergence and coalescence of like-polarities, increasing both negative and positive flux at a similar, approximately constant rate of 4×10^{20} Mx h^{-1} (Mx: maxwell). This phase lasts approximately until t=50 h, and it is followed by a second phase when, together with the emergence, also a major flux cancellation event can be seen to occur lasting about 20 h at the neutral line between the leading-positive and the negative polarity (although the latter emergence is not apparent in the evolution due to the relatively small amount of flux involved, see Figure 2). Flares are registered both at the beginning (entry 1 in Table 1) and at the end (entries 2 and 3 in Table 1) of this emergence/cancellation phase.

Until t=80 h, the rate of emergence is roughly constant, with that of the negative flux larger than the positive one. As a result, the relative imbalance is progressively decreasing as the unsigned flux grows. A change in the rate of emergence can be clearly seen in Figure 2 starting at around 80 h, or shortly before. After that time, the rate of emergence of negative flux clearly decreases, whereas that of the positive one, after a slight slow down over a duration of 10 h, increases to a clearly higher rate than that of the negative flux. After 105 h, the lines representing the positive and negative fluxes cross each other and the imbalance sign reverses, with now more positive flux than negative. The time of the inversion of the sign of the imbalance is definitely biased by the presence of the, predominantly negative, old flux, and it is therefore not accurately estimated. However, this crossing point happens far from the time of the central meridian passage, which instead occurs at about $t = 62$ h, and it is represented in Figure 2 by the vertical dash-dotted line. Therefore, the inversion in the sign of the imbalance may only partially be due to a change in the projection effect in the presence of emerging (horizontal) fields (Green *et al.*, 2003). This is a first indication of a global change in the emergence process that starts after $t = 80$ h, when the rate of emergence of positive flux becomes larger than that of negative one. An examination of the MDI magnetograms (Figures 1d and 1e) reveals that, at approximately this time, an important new flux emergence occurs in the east of the firstly emerged bipole, now with correct orientation for Hale's law. From this point until the end of the studied period, the positive flux increases at a much faster rate than the negative one, the latter even starting to decrease after $t = 120$ h. This final phase is marked by the most energetic eruptive events in our series (entries 5 and 6 in Table 1).

The configuration that the AR attains at the end of the observed time span (Figure 1f) is given by a central, elongated negative flux concentration in between two positive-polarity concentrations. It is to be expected that such a configuration hosts neighbouring field lines that, from the negative polarity, connect on the two positive on opposite sides. Even though we do not study the topological configuration of this AR here, it is likely that a quasi-separatrix layer (Démoulin

et al., 1996) is located within the central, negative flux concentration, facilitating the formation of currents there, and possibly the generation of flares.

After this time (t = 140 h), the AR approaches the limb, and cannot be accurately followed any more. Therefore, we stop the analysis at this point, although the AR was observed to generate a few more M-class events in the following three days (entries 7 to 11 in Table 1).

4. Computation of the Magnetic Helicity Accumulated in Corona

In order to compute the photospheric magnetic helicity flux during the selected time interval, we constructed the mean magnetogram corresponding to the average between two consecutive magnetograms, and we measured the horizontal velocity fields with the differential affine velocity estimator (DAVE) method (Schuck, 2005), using a full-width-at-half maximum of the apodization window of 19.80 arcsec and a time interval of 96 min. Then, we used the velocity fields to compute the maps of the magnetic helicity flux and the accumulation of magnetic helicity in the corona by applying Equations (18) and (19) of Pariat *et al.* (2005), which do not require the knowledge of the transverse magnetic field at the photosphere. We neglected the magnetic field below 20 G (gauss). In the left panel of Figure 3, with the orange line, we report the magnetic helicity accumulation during the selected time interval. The time when the flares and the associated CMEs occurred are indicated by vertical lines. The initial helicity is set to zero, in accordance with the time series starting before the actual emergence. The pre-existing helicity content of the AR is not known, but it should be finite, since in the first 10 to 15 h helicity is seen to decrease very slightly in time, as a manifestation of the erosion of the pre-existing AR. We neglected this arguably small initial contribution in the analysis that follows.

Figure 3 shows that AR NOAA 10365 is characterised by a positive magnetic helicity flux during the whole selected time interval, reaching at maximum $\approx 2.1 \times 10^{43}$ Mx^2. The helicity starts to increase 10 to 15 h after the beginning of the AR emergence, and enters a clear linear phase after t = 65 h. This linear phase roughly corresponds to the second phase of emergence, when large flux cancellation in the core of the AR takes place (see Section 3). A significant variation in the magnetic helicity flux occurs before the X1.3 GOES class flare after approximately 80 h from the beginning of the observation interval (see the variation in the slope of the orange curve in the left panel of Figure 3). This variation is the counterpart on the accumulated helicity of a similar variation in the emergence process around that time that was reported above. The accumulated helicity levels off after 120 h, apparently after the occurrence of the last considered event. From the flux evolution analysis of Section 3, we can link this phase to the decrease of the negative flux injection rate.

5. Linear Theory with Flare Intensity Scaling

In the linear force-free field approximation, the magnetic helicity (H_m) and free magnetic energy ($\mathcal{E}_\mathrm{c}$) in the semi-space above the photospheric plane ($z = 0$) are

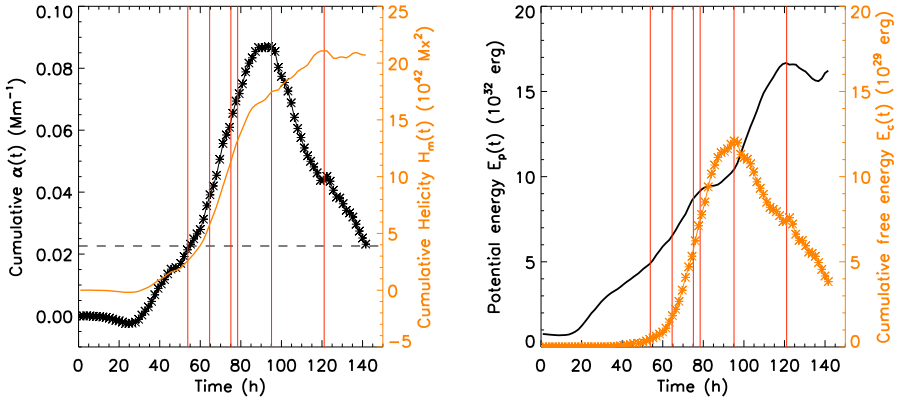

Figure 3. Left: cumulative α (black stars) and magnetic helicity (orange line), as a function of time. $\alpha(t)$ is derived from the cumulative helicity using Equation(2). The horizontal dashed line is the value of $\alpha_{\rm max}$ (see text). Right: Energy of the potential field (black line) and free energy (orange stars), as a function of time. In both plots, the red vertical lines indicate the peak time of the flares in our time series.

given by (Georgoulis and LaBonte, 2007):

$$H_{\rm m} = 8\pi\mathcal{F}_{\rm l} d^2 \alpha \mathcal{E}_{\rm p}\,, \tag{2}$$

$$\mathcal{E}_{\rm c} = \mathcal{F}_{\rm l} d^2 \alpha^2 \mathcal{E}_{\rm p}\,, \tag{3}$$

where d is the (linear) size of the pixel, and $\mathcal{F}_{\rm l}$ is a function of the Fourier components of $B_z(z=0)$ and of the wave vector's components, but it does not depend on α. $\mathcal{E}_{\rm p}$ is the energy of the potential field, which can be conveniently expressed by the surface integral

$$\mathcal{E}_{\rm p} = \frac{1}{8\pi}\int_{z=0} \boldsymbol{z}\cdot(\boldsymbol{B}_{\rm p}\times\boldsymbol{A}_{\rm p})\,{\rm d}x{\rm d}y\,, \tag{4}$$

with the horizontal components of the potential field ($\boldsymbol{B}_{\rm p}$) and of its vector potential ($\boldsymbol{A}_{\rm p}$) at $z=0$ given by the usual Fourier solution of the force-free field equations.

Equations (2) and (3) are in fact a linearised version of more general ones, where the dependence of $H_{\rm m}$ and $\mathcal{E}_{\rm c}$ on α remains implicit (*cf.* Equation (34a) and (34b) in Georgoulis and LaBonte (2007)). The difference between the linearized and general equations is shown in Figure 4 at one particular time during the time interval analysed. For the general equations (connected crosses in Figure 4), the presence of a resonance at $\alpha = \alpha_{\rm max}$ makes the helicity (and the energy) divergent as $\alpha_{\rm max}$ is approached, as well known. The resonant value $\alpha_{\rm max}$ is basically the inverse of the size of the domain, which is given by the linear size of the observed area plus the padding (with zero values) that is normally employed to avoid aliasing in the Fourier transform. However, the resonance is an artefact of the periodicity implied by the Fourier analysis, and it is not

physical (Green *et al.*, 2002). In the first place, for each individual value of $\alpha_{\rm max}$, the linearized formulae (solid lines in Figure 4) can reproduce the helicity far from the (unphysical) resonance. In this sense, the linearized formulae can be considered to provide a lower limit to the (LFFF) values of energy and helicity. Second, the linearized formulae are almost unaffected by different values of $\alpha_{\rm max}$ (the four solid lines practically overlap each other), *i.e.* they are not affected by the width of the padding area employed to compute Fourier transforms. Hence, in the analysis that follows, we employ no padding in order to have the largest possible reference value of $\alpha_{\rm max}$. Moreover, we are allowed to use the linearized formulae, Equations (2)-(4), also beyond the nominal $\alpha_{\rm max}$ value.

Within the validity of the LFFF theory, helicity, free energy, and α are related through Equations (2) and (3). Therefore, they can be derived from one another. In particular, by using Equation (2) we can compute the value of α that corresponds to each value of the accumulated helicity as derived from the observations (see Section 4). The potential field energy $\mathcal{E}_{\rm p}$ and $\mathcal{F}_{\rm l}$ in Equation (2) are computed directly from the observations using Equation (4) in this paper and Equation (34b) in Georgoulis and LaBonte (2007), respectively. We obtain in this way a "cumulative α" from the cumulative helicity, as a function of time, shown as black stars in the left panel of Figure 3. Similarly, for each value of α, we can also compute the corresponding free energy according to Equation (3). The corresponding plot is shown together with the time evolution of the potential magnetic energy in the right panel of Figure 3.

First of all, the time evolution of the potential field energy reflects the emergence process as already described in terms of fluxes in Section 3, as it might be expected. Similar phases can be identified, with the only difference being the very final evolution where the decrease of the negative flux yields a levelling off of the energy similarly to that in the accumulated helicity (*cf.* left panel of Figure 3).

Secondly, $\alpha(t)$ follows a similar behaviour in time as the accumulated helicity and the potential energy until $t = 80$ h, but it differs sensibly from both afterwards. Shortly before the first powerful X-class flare (event 5 in Table 1), the AR evolution changes behaviour dramatically, showing a decrease in $\alpha(t)$. We interpret this result as a consequence of the observed significant flux emergence that starts to globally re-arrange the AR and, as a consequence, triggers the first X-class flare. Apart from the above, no major change is registered either in $H_{\rm m}(t)$ or in $\alpha(t)$ at the time of the flares. This is equally true for the potential field energy (black line in the right panel of Figure 3).

The sudden increase in $\mathcal{E}_{\rm p}$ after the X-class flare due to the new emergence is at the origin of the corresponding decrease of α: Since $H_{\rm m}(t)$ is seen to slow down during the emergence, whereas the flux strongly increases, then α must decrease in order to keep the (linear) relation $H \sim \alpha\Phi^2$ (Leamon, Canfield, and Jones, 2004). Another way to look at the same mechanism is the temporal evolution of $\mathcal{F}_{\rm l}$ shown in Figure 2. The quantity $\mathcal{F}_{\rm l}$ is a combination of the Fourier amplitudes of the vertical fields and wavelengths, which has larger values when the field is predominantly on larger scales. In Figure 2 the main emergence is clearly seen in the rapid decrease of $\mathcal{F}_{\rm l}$ between $t = 10$ and $t = 25$ h, showing that the photospheric field in this phase is characterised by the emergence of

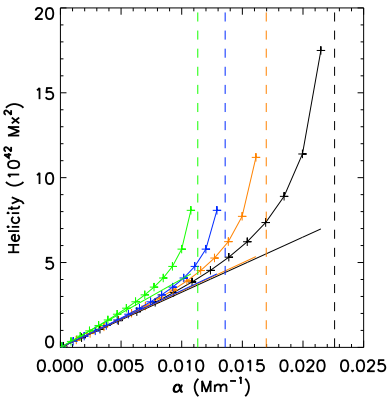

Figure 4. Magnetic helicity for the 28 May at 13:36 UT magnetogram, as a function of α, for different widths of padding, *i.e.* of $\alpha_{\max}$, here represented by the vertical dashed lines. The number of pixels per side used for padding are [135, 90, 45, 0] for the green, blue, orange, and black lines, respectively. The solid lines are computed using the linearized formulae, Equation (2), whereas the connected crosses are computed with the more general Equation (34b) in Georgoulis and LaBonte (2007).

small-scale field. As the emergence process continues, similar phases can be identified as in the plot of the negative and positive fluxes, until $t = 95$ h. After this time, $\mathcal{F}_\mathrm{l}$ starts increasing rapidly again, indicating a marked change in the emergence process, which is now characterised by a field with energy on larger and larger scales. This process is so marked that, despite the increasing values of the accumulated helicity, the corresponding value of $\alpha \propto H_\mathrm{m}/(\mathcal{E}_\mathrm{p}\mathcal{F}_\mathrm{l})$ actually decreases in time.

Finally, the free energy (orange stars in the right panel of Figure 3) follows the α^2-law of Equation (3). As a consequence, the accumulation of free energy is very slow during the initial phases of emergence, reaching significant nonzero values only shortly before the first M-class flare ($t \simeq 50$ h). Again, after a slowly accelerating rise, a decreasing phase is attained when re-arrangement of the field takes place as a consequence of the second episode of large flux emergence in the AR.

The above description of the AR evolution is based on (and has the validity of) a combination of photospheric observations and the LFFF model of the coronal field. In particular, the change in the coronal field leading to the first X-class flare, as well as the re-arrangement of the field as a consequence of it, are very likely to be highly non-linear processes. Therefore, the evolution of the free energy of the AR close to and following the first X-class flare cannot be entirely trusted. However, the analysis presented above is for a much longer span of time because the evolution of the accumulated helicity and of the magnetic energy of the potential field are based on photospheric signals only, and can be studied independently from the LFFF approximation (*i.e.* α and $\mathcal{E}_\mathrm{c}$).

5.1. Flare Intensity Scaling

An additional limitation of the above analysis is that none of the quantities plotted in Figure 3 takes into account the occurrences of CMEs, which remove (free) energy and helicity from the system. The question is then how to include the effect of CMEs in the analysis, at least approximately, and how to estimate the drop in α that is expected to result from each CME. Given Equation (3), this is equivalent to find an estimate of the amount of free energy liberated in each event. Such an estimate is not easily attainable from the available observations, which are essentially based on the GOES values of the energy fluxes associated with each event. However, making the assumption that all events are generated by the same mechanism, we can argue that the GOES measurements $\Phi_{\rm GOES}$ are a proxy of the liberated energy in each event. In particular, we assume that the fraction of the free energy liberated in each event , $\delta\mathcal{E}_{\rm c}|_{\rm CME}$, is proportional to the time-integrated X-ray flux, $\Delta\mathcal{E}_{\rm c}$:

$$\delta\mathcal{E}_{\rm c}|_{\rm CME} \propto \Delta\mathcal{E}_c = \int_{t_{\rm start}}^{t_{\rm end}} \Phi_{\rm GOES} \simeq 0.5(t_{\rm end} - t_{\rm start})\Phi_{\rm GOES}^{\rm peak}\,, \qquad (5)$$

where $\Phi_{\rm GOES}^{\rm peak}$ is the peak X-ray flux from Table 1 expressed in $\mathrm{erg\,cm^{-2}\,s^{-1}}$. The integration of the GOES signal in time is performed for a simple linear ramp-up (from start to peak) and ramp-down (from peak to end) using the values in Table 1. Note that the proxy $\Delta\mathcal{E}_{\rm c}$ does not provide the value of the liberated energy in each event, but rather its relative value within the group of flares studied. The values taken by this proxy are shown in the rightmost column in Table 1 for the six considered events.

Finally, we can use Equation (3) to derive from our proxy the drop in α between two consecutive events i and i+1. In order to do so, let us introduce $\Delta\alpha_i$ as the drop in α due the i-th event. The corresponding drop in the energy according to Equation (3) is $\Delta\mathcal{E}_{{\rm c},i} = (d^2\mathcal{F}_{\rm l}\mathcal{E}_{\rm p})_i(\Delta\alpha_i^2 - 2\alpha_i\Delta\alpha_i)/4\pi$, where α_i is to be interpreted as the value of α immediately before the i-th event. The values of $\Delta\mathcal{E}_{{\rm c},i}$ for the considered events are reported in the rightmost column of Table 1. Implicitly, we have also assumed that the normal field, and therefore $\mathcal{F}_{\rm l}$ and $\mathcal{E}_{\rm p}$, are not changed during a single event, but only between the events. Now, we can consider the ratio $\Delta\mathcal{E}_{{\rm c},i}/\Delta\mathcal{E}_{{\rm c},i+1}$ of the drop in the energy of two consecutive events, and solve for $\Delta\alpha_{i+1}/\alpha_{i+1}$ to obtain:

$$\frac{\Delta\alpha_{i+1}}{\alpha_{i+1}} = 1 \pm \sqrt{1 + \frac{(\alpha^2\mathcal{F}_{\rm l}\mathcal{E}_{\rm p})_i}{(\alpha^2\mathcal{F}_{\rm l}\mathcal{E}_{\rm p})_{i+1}}\frac{\Delta\mathcal{E}_{{\rm c},i+1}}{\Delta\mathcal{E}_{{\rm c},i}}\left\{\left(\frac{\Delta\alpha_i}{\alpha_i}\right)^2 - 2\left(\frac{\Delta\alpha_i}{\alpha_i}\right)\right\}}\,, \qquad (6)$$

expressing the drop in α in the i+1 event as a function of $\Delta\mathcal{E}_{{\rm c},i+1}/\Delta\mathcal{E}_{{\rm c},i}$, which can be estimated using the GOES proxy Equation (5), and of quantities derived from the magnetograms at $t = t_i$ and $t = t_{i+1}$. The sign on the right-hand side of Equation (6) is chosen such as to decrease the value of α_{i+1}.

With reference to the black curve in the left panel of Figure 3, we then proceed as follows: starting with the potential field at $t = 0$, we need to assume a value

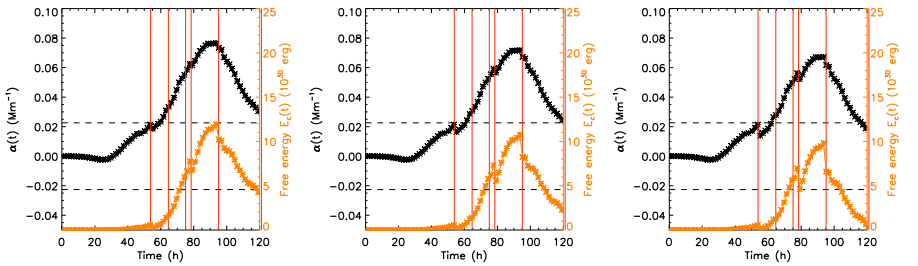

Figure 5. CME-normalized α (black stars) and free energy (orange crosses), as a function of time, for the three values of the free parameter $\Delta\alpha_1 = \alpha_1 \times [0.2, 0.3, 0.4]$ (from left to right). The horizontal dashed lines show the value of $\alpha_{\max}$. In all plots, the red vertical lines indicate the time of the peak of the flares (1-5) in the time series (see Table 1).

for the drop in α due to the first event ($\Delta\alpha_1$) on 26 May 2003 at 05:34 UT, corresponding to $t_1 = 54$ h. Then, from $\Delta\mathcal{E}_{c,2}/\Delta\mathcal{E}_{c,1} = 9/16$, we compute the drop $\Delta\alpha_2$ from Equation (6) for the second event (at $t_2 = 65$ h), and we subtract this value from the $\alpha(t)$-plot in the left panel of Figure 3 for all $t \geq t_2$. The procedure is then repeated for all successive events. For the reasons explained at the end of the previous Section, we stop this analysis shortly after the occurrence of the first X-class flare.

Figure 5 shows the values of $\alpha(t)$ and $\mathcal{E}_c(t)$ resulting from the application of the method, for three values of the free parameter $\Delta\alpha_1/\alpha_1$ equal to 40%, 30%, and 20%. The orange curves in the three panels of Figure 5 show that, for larger and larger values of the free parameter $\Delta\alpha_1$, the value of $\mathcal{E}_c$ at the end of the time series is closer and closer to zero. Since the free energy must remain positive throughout the evolution, this sets an upper limit to $\Delta\alpha_1/\alpha_1$, in the present case equal to 0.44. Of course such a value depends on the initial value $\alpha(t = 0)$, and on the cutoff time that we have used in the time series (in the case of Figure 5 equal to 120 h). The existence of such constrain on $\Delta\alpha_1$ is, however, guaranteed, and it can be reached if the AR at the end of the analysed period has already attained a bipolar, essentially potential configuration. Since the relative importance of each event is linked to the amplitude of the free parameter $\Delta\alpha_1$, the smaller the latter, the smaller are the drops in $\alpha(t)$. For $\Delta\alpha_1 = 0$, the curves in the left panel of Figure 3 are recovered.

In general, the method applied in this study has two free parameters. The first one is $\alpha(t = 0)$. This unknown is inherited from the computation of the helicity flux, where the initial helicity (*i.e.*, the value of $H_m(t = 0)$ in the left panel of Figure 3) is not determined by that method. We set approximately $H_m(t = 0) = 0$, and, hence, $\alpha(t = 0) = 0$, because we follow the emergence from the very beginning. The second free parameter, more properly belonging to our method, is the drop in α due to one of the events occurring during the time series. The latter can be determined, for instance, by comparisons of EUV images with field lines of extrapolated magnetic fields obtained for different values of α, in a regime where the LFFF approximation is reasonably expected to hold. Since the flare energy proxy does not fix the value of α without that additional piece of information, we qualified our method only as a *partial* alternative of constraining

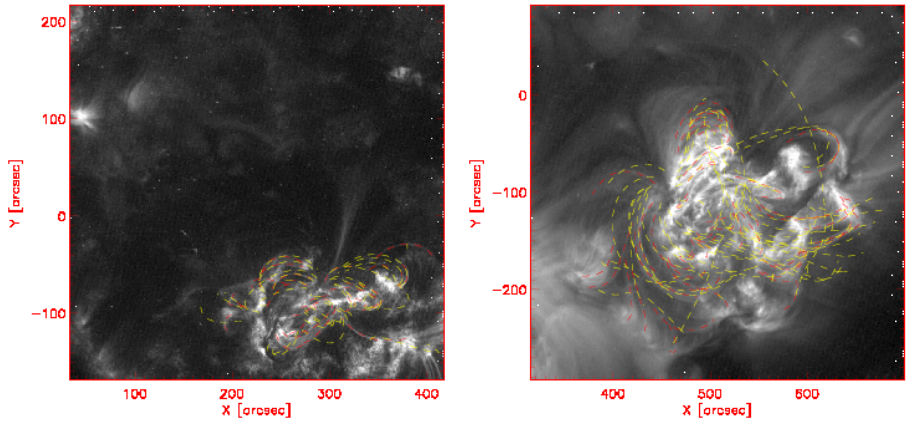

Figure 6. Set of identified loops (red dashed lines) and of the correspondent extrapolated field lines (yellow dashed lines) in the best-matching $\alpha_{\rm cor}$ extrapolation, overlaid to the TRACE 171 Å images, at $t = 91$ (left) and $t = 118$ (right).

α. On the other hand, our method, supplied by the value of α at one time only (or at two, if $H_{\rm m}(t = 0)$ cannot be neglected), provides the value of α at all times of observation as determined by the combination of the photospheric flux evolution and of a proxy of the coronal activity. In Section 6 an example of fixing the free parameter $\Delta\alpha_1$ by matching EUV loops is given.

The main assumption of the method, besides the LFFF approximation, is that all considered events can be thought of as being produced by the same mechanism, such that it makes sense to estimate their relative energies through their signature in the GOES observations only. In the application reported here, there is a marked change in the AR evolution occurring after $t = 80$ h that was described in terms of magnetic flux, helicity, and free energy. Such a change was related to a second major flux emergence with Hale orientation adjacent to the non-Hale first flux emergence site, which was likely to be the cause of the very powerful X-class flare following shortly afterwards. Such a major reconfiguration of the coronal field can hardly be satisfactorily described within the regime of LFFF theory, and, therefore, our analysis must stop shortly after the occurrence of this event. This is the main reason because, in this section, we considered only the first five events in Figure 5.

6. Comparison with Coronal α

One of the methods for fixing the free parameter alpha in the LFFF theory applied to a magnetogram at a given time is to find which value produces field lines that best match observed loops in EUV or SXR images (*e.g.*, Green *et al.*, 2002; Brunette *et al.*, 2004; Lim *et al.*, 2007). We apply a similar method here, in the implementation closest to that of van Ballegooijen (2004), while being a modification of the method describe in Malanushenko *et al.* (2009). While Malanushenko *et al.* (2009) compared each loop individually against a set of

constant-α field lines for different values of alpha, here we look for a constant-alpha field that best describes the entire ensemble of observed loops. For each given constant-alpha field we first find a best match for every loop. To do that, we trace field lines from a set of locations in the domain along the line of sight s, which projects onto the center of the loop in the plane of sky an calculate the average distance $d(s)$ between these field lines an the loop, in the manner described in Malanushenko *et al.* (2009). For the purpose of the current study, the best-fitting field line is considered to be at the lowest minimum of $d(s)$. For each constant-alpha field, this procedure yields a set of discrepancies d_i from an i-th loop and a best-fitting field line. The median of this distances $\overline{d_i}$ is treated as a single parameter which quantifies how well does a given constant-alpha field match the observed ensemble of the observed loops.

During the observation interval considered here, only two *Transition Region and Coronal Explorer* (TRACE; Handy *et al.*, 1999) images at 171 Å were taken, namely on 27 May at 19:24 UT ($t = 91$), and on 28 May at 22:23 UT ($t = 118$). Of the two images, the first one has remarkably less contrast and includes only partially the region of interest, see Figure 6. The number of loops that could be identified in the TRACE image in this case is about half that at $t = 118$, namely 28 and 53 in the two cases. We used the closest MDI magnetograms (12 min earlier for the first case, co-temporal in the second) to compute the magnetic fields correspondent to different values of α. Using the procedure described above, a median distance diagram was constructed for each case shown in Figure 7, and the best value of α was determined as that corresponding to the minimum of the median distance curve. We refer to the value of α determined in this way as $\alpha_{\rm cor}$, since it is determined essentially by comparisons with coronal loops.

In the first place, we notice that, on average, the value of the median distance is lower for the earlier image ($t = 91$ h) than for the later one ($t = 118$ h). Hence, for the sets of identified loops in the two cases, the linear extrapolation is able to better match the earlier case than the later one. On this grounds, we should expect $\alpha_{\rm cor}$ to be a better match of the coronal field at $t = 91$ than at $t = 118$. On the other hand, the curve relative to $t = 91$ h has three minima with very similar values of the median distance, *i.e.* of the quality of the matching. In such a case, the value of $\alpha_{\rm cor}$ is essentially undetermined. However, for the sake of comparison with our method, we consider in the following the absolute minimum resulting from the minimization procedure.

As for the actual values, we found that the TRACE loops, at the two available times $t = 91$ and $t = 118$ h, are best represented by the values $\alpha_{\rm cor} = 0.003$ Mm^{-1} and $\alpha_{\rm cor} = 0.015$ Mm^{-1}, respectively. The resulting field lines that, according to minimization procedure, fit best the TRACE loops are shown in Figure 6 for the two considered times.

If we compare the coronal values $\alpha_{\rm cor}$ with the accumulated α derived from the photospheric evolution at the same time (see Figure 3, before the application of the flare energy scaling, for simplicity), we find that our accumulated values are 22 and 2 times larger than the $\alpha_{\rm cor}$, respectively. The latter value is in line with Gosain *et al.* (2014) for photospheric versus chromospheric ratios of α, and is essentially consistent with the accumulated value derived from the

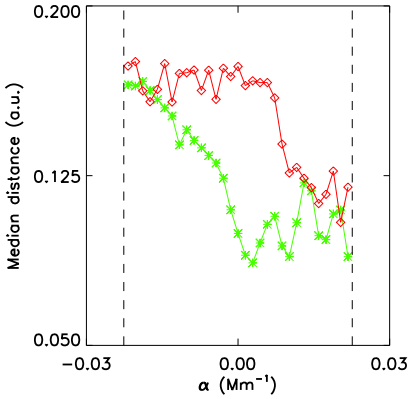

Figure 7. Median distance $\overline{d_i}$ between TRACE loops and field lines, as defined in Section 6, as a function of α, for 27 May at 19:24 UT (green asterisks) and 28 May at 22:23 UT (red diamonds). The vertical dashed lines indicates the values of $\pm\alpha_{\max}$.

photospheric evolution. On the other hand, the value of $\alpha_{\rm cor}$ at $t = 81$ h is very small. Considering the corresponding free energies, which, from Equation (3), scale as α^2, the values obtained with the $\alpha_{\rm cor}$ at $t = 91$ and 118 h are 2.5×10^{27} erg and 1.95×10^{29} erg, respectively.

The former is unrealistically small, especially considering that it corresponds to a time just 3 h before an X-class flare, whereas our method gives values that are at their maximum there. Such an apparently contradictory result of a very good fitting which produces an unrealistic value of α is probably due to the poor quality of the TRACE image at $t = 91$ h, which shows only the most external potential loops. Hence, it is an example of the critical dependence of the loop-matching method on the quality of coronal loops image. On the other hand, it is most likely that the AR is in a nonlinear regime at this stage, in which case a single value of $\alpha_{\rm cor}$ cannot fit the coronal field in the entire volume. The presence of three substantially equivalent fitting values of $\alpha_{\rm cor}$ may indicate that the field at this particular time cannot be modeled using the LFFF approximation.

On the other hand, when the TRACE image is good enough, as at $t = 118$, the value of $\alpha_{\rm cor}(t = 118)$ is close to the value obtained at that time by our model, in particular for $\Delta\alpha_1/\alpha_1 = 0.4$, which then fixes $\Delta\alpha_1$ in the flare energy scaling modification of the accumulated α.

Considering the $\Delta\alpha_1/\alpha_1 = 0.4$ case as the one matching best the configuration of the AR at $t = 118$ h, we have therefore obtained the evolution of α over five days of observations, including the effect of flares/CMEs as proxied by the GOES measurements. In this way, LFFF extrapolations are consistently related throughout the considered span of time, rather than adjusted only on the basis of unrelated comparisons with EUV images at different times.

7. Conclusions

Using the LFFF approximation, we deduced the temporal evolution of the force-free parameter α and of the free energy $\mathcal{E}_c$ from measurements of the magnetic helicity accumulation in the corona in the AR NOAA 10365, where several flares and CMEs occurred during the selected time interval. Taking into account that the occurrences of CMEs remove energy and helicity from the system, we used an approximation method to quantify the amount of energy released in each eruptive event and to deduce the energy budget of the AR over a five-days time interval. We assumed that the energy liberated in each event was proportional to the GOES class event, integrated over the time of its duration. As a consequence of the relation between (free) energy and helicity in the LFFF approximation, the above assumption also fixed the amount of helicity removed in each event. This procedure reduces the number of unknown variables from six (the initial value and the effect on α of the five CMEs observed during the considered time interval) to two: $\alpha(t = 0)$ and the drop in α due to the first event, $\Delta\alpha_1$. In agreement with the observation that the AR has been formed within the dispersed and eroded bipolar structure of an old one, and due to the gradual increase of α before the first event, we assumed that $\alpha(t = 0) = 0$. The second free parameter, $\Delta\alpha_1$, was determined using the more traditional method of comparing field lines of extrapolated magnetic fields obtained for different values of α with coronal EUV images.

The method of fixing α that we present here exploits the observed temporal evolution of the magnetic flux. Therefore, the obtained values of α at different times are related to each other by the photospheric evolution on the one hand, and by the coronal dynamic as proxied by the GOES fluxes on the other. A comparison with the loop-matching method of fixing α at each time independently showed that the proposed method may be helpful to avoid unrealistic or undetermined values that originate from an insufficient quality of the image used to identify coronal loops.

Due to the different duration of the events occurring in the considered AR, the GOES proxy of released energy $\Delta\mathcal{E}_c$ has comparable values for the first three events (all M-class) and for the following two (M1.6 and X1.3 class), the latter being more than three times larger than the former. In addition, the energy plot in Figure 5 shows that it does not take the same drop in α to produce a similar drop in the free energy at different stages of evolution. Indeed, the LFFF approximation yields:

$$\Delta\mathcal{E}_c = -2\mathcal{F}_l d^2 \mathcal{E}_p \alpha \left(1 - \frac{1}{2}\frac{\Delta\alpha}{\alpha}\right) \Delta\alpha \simeq -\frac{1}{4\pi} H_m \Delta\alpha \,, \tag{7}$$

which, in terms of free energy, implies that $\Delta\mathcal{E}_c/\mathcal{E}_c \simeq -2(\Delta\alpha/\alpha)$. Therefore, the larger is the value of H_m, the smaller is the $\Delta\alpha$ required to produce a given drop in free energy. For this reason, on the one hand, the first three events (all of class lower than M2) appear to affect $\alpha(t)$ less and less as the evolution proceeds. On the other hand, the following two events, which, according to our proxy, are energetically comparable and more than three times larger than the first three, do not modify the value of $\alpha(t)$ in similar proportions.

Within the applicability limits of LFFF theory, the method presented here offers a partial alternative to the more traditional one of constraining the force-free parameter α by comparison with EUV images. Rather than performing such a comparison independently at each required time and obtaining values of α that are unrelated with each other, the method presented here provides a time evolution of α that is consistent with the energy drops due to flare/CME events as measured and scaled by the X-ray flux from the GOES satellite.

Acknowledgements The research leading to these results has received funding from the European Commissions Seventh Framework Programme under the grant agreements n^o 284461 (eHEROES project), n^o 312495 (SOLARNET project), and from n^o 263340 (SWIFF project). LvDG's work was supported by the Hungarian Research grants OTKA K-081421 and K-109276, and the STFC Consolidated Grant ST/H00260/1. PR, IE, FG, FZ work was partially supported by the INAF grant PRIN-INAF-2010. The SOHO/LASCO CME catalog is generated and maintained at the CDAW Data Center by NASA and The Catholic University of America in cooperation with the Naval Research Laboratory. SOHO is a project of international cooperation between ESA and NASA. TRACE is a mission of the Stanford-Lockheed Institute for Space Research, and part of the NASA Small Explorer program.

References

Alissandrakis, C.E.: 1981, *Astron. Astrophys.* **100**, 197.
Aulanier, G., Schmieder, B.: 2002, *Astron. Astrophys.* **386**, 1106.
Berger, M.A.: 1984, *Geophys. Astrophys. Fluid Dyn.* **30**, 79.
Berger, M.A.: 1985, *Astrophys. J. Suppl.* **59**, 433.
Brueckner, G. E., Howard, R. A., Koomen, M. J., Korendyke, C. M., Michels, D. J., Moses, J. D., *et al.*: 1995, *Solar Phys.* **162**, 357.
Burnette, A. B., Canfield, R. C., Pevtsov, A. A.: 2004, *Astrophys. J.* **606**, 565.
Chae, J. , Wang, H. , Qiu, J. , Goode, P. R. , Strous, L. , Yun, H. S.: 2001, *Astrophys. J.* **560**, 476.
Démoulin, P., Hénoux, J. C., Priest, E. R., Mandrini, C. H. : 1996, *Astron. Astrophys.* **308**, 643.
Démoulin, P., Mandrini, C. H., van Driel-Gesztelyi, L., Thompson, B. J., Plunkett, S., Kovári, Z., Aulanier, G., Young, A.: 2002, *Astron. Astrophys.* **382**, 650.
DeRosa, M. L. , Schrijver, C. J. , Barnes, G. , Leka, K. D. , Lites, B. W. , Aschwanden, M. J., *et al.*: 2009, *Astrophys. J.* **696**, 1780.
Forbes, T.G.: 1984, *J. Geophys. Res.* **105**, 23153.
Georgoulis, M. K., LaBonte, B. J.: 2007, *Astrophys. J.* **671**, 1034.
Gosain, S., Démoulin, P., López Fuentes, M.: 2014, *Astrophys. J.* **793**, 15.
Green, L. M., López Fuentes, M., Mandrini, C. H., Démoulin, P., van Driel-Gesztelyi, L., Culhane, J. L.: 2002, *Solar Phys.* **208**, 43.
Green, L. M., Démoulin, P., Mandrini, C. H., Van Driel-Gesztelyi, L.: 2003, *Solar Phys.* **215**, 307.
Handy, B. N., Acton, L. W., Kankelborg, C. C., Wolfson, C. J., Bruner, M. E., Caravalho, R., *et al.* : 1999, *Solar Phys.* **187**, 229.
Howard, R. F., Harvey, J. W., Forgach, S.: 1990, *Solar Phys.* **130**, 295.
Kusano, K., Maeshiro, T., Yokoyama, T., Sakurai, T.: 2002, *Astrophys. J.* **577**, 501.
Leamon, R.J., Canfield, R.C., Jones, S.L., Lambkin, K., Lundberg, B.J., Pevtsov, A.A.: 2004, *J. Geophys. Res.* **109**, 5106.
Lim, E. K., Jeong, H., Chae, J., Moon, Y. J.: 2007, *Astrophys. J.* **656**, 1167.
Luoni, M.L., Démoulin, P., Mandrini, C. H., van Driel-Gesztelyi, L.: 2011, *Solar Phys.* **270**, 45.
Malanushenko, A., Longcope, D. W., McKenzie, D. E.: 2009, *Astrophys. J.* **707**, 1044.

Mandrini, C. H., Démoulin, P., van Driel-Gesztelyi, L., Schmieder, B., Cauzzi, G., Hofmann, A.: 1996, *Solar Phys.* **168**, 115.
Mandrini, C. H., Démoulin, P., Bagala, L. G., van Driel-Gesztelyi, L., Hénoux, J.-C., Schmieder, B., Rovira, M.G.: 1997, *Solar Phys.* **174**, 229.
Nagakawa, Y., Raadu, M. A.: 1972, *Solar Phys.* **25**, 137.
Pariat, E. , Aulanier, G. , Schmieder, B. , Georgoulis, M. K. , Rust, D. M. , Bernasconi, P. N.: 2004, *Astrophys. J.* **614**, 1099.
Pariat, E., Démoulin, P., Berger, M.A.: 2005, *Astron. Astrophys.* **439**, 1191.
Petsov, A. A., Canfield, R. C., Metcalf, T. R.: 1995, *Astrophys. J. Lett.* **440**, L109
Romano, P., Contarino, L., Zuccarello, F.: 2003, *Solar Phys.* **214**, 313.
Romano, P., Pariat, E., Sicari, M., Zuccarello, F.: 2011, *Astron. Astrophys.* **525**, 13.
Sakurai, T.: 1989, *Space Sci. Rev.* **51**, 11.
Schmieder, B., Démoulin, P., Aulanier, G., Golub, L.: 1996, *Astrophys. J.* **467**, 881.
Scherrer, P.H., Bogart, R.S., Bush, R.I., Hoeksema, J.T., Kosovichev, A.G., Schou, *et al.*: 1995, *Solar Phys.* **162**, 129.
Schuck, P. W.: 2005, *Astrophys. J. Lett.* **632**, L53.
Seehafer, N.: 1978, *Solar Phys.* **58**, 215.
Török, T., Kliem, B.: 2005, *Astrophys. J. Lett.***630**, L97.
van Ballegooijen, A. A: 2004, *Astrophys. J.***612**, 519.
Wiegelmann, T.G.: 2008, *J. Geophys. Res.* **113**, 3.
Wiegelmann, T., Sakurai T.: 2012, *Living Rev. Solar Phys.* **9** (5), http://solarphysics.livingreviews.org/Articles/lrsp-2012-5/